

VIP Very Important Paper

www.batteries-supercaps.org

Harnessing Regenerated Graphite from Spent Lithium-Ion Batteries to Enhance the Performance of Sulfur Cathode in Lithium-Sulfur Batteries

Huiying Sheng,*^[a] Magdalena Graczyk-Zajac,*^[a, b] Honghong Tian,^[a] Fangmu Qu,^[a] Yaohao Zhang,^[a] Michael Dürrschnabel,^[c] Anke Weidenkaff,^[a, d] and Ralf Riedel^[a]

In this work, a facile hydrometallurgical approach combined with heat treatment has been adopted to recycle spent graphite from retired lithium-ion battery cells. Graphite regenerated with 18 M H₂SO₄ leaching leads to a high specific surface area, significant porosity and small crystallite size. The regenerated graphite has been infiltrated with sulfur under solvothermal conditions at 160°C. The sample containing 68 wt % of sulfur recovers a capacity of 224 mAh/g after 100 cycles. Furthermore, the electrode with a higher sulfur content of

84 wt %, recuperates the specific discharging capacity of 207 mAh/g after 100 cycles. After the initial fading during the first 5–10 cycles, the cathodes based on regenerated graphite demonstrate stable cycling behavior. This research not only offers an accessible and scalable method for regenerating graphite from spent LIBs but also demonstrates a new application of the regenerated graphite in LSBs, showcasing outstanding electrochemical performance.

Introduction

Since 1991, secondary lithium-ion batteries (LIBs) have emerged as a highly promising energy storage solution, facilitating the load shift in a clean energy production and utilization and playing a pivotal role in the development of portable devices and electric vehicles.^[1,2] With the widespread commercialization of LIBs, the proper disposal of end-of-life batteries and alleviating of the shortage of raw material resources have become urgent and critical tasks to meet future demands.^[3] Recycling and regeneration of spent LIBs can eliminate the

landfills and incineration. Moreover, the overload mining, extraction and refining can be reduced by reuse the elements.^[4] The influence of uneven distribution of resources can be reduced and significant economic benefits are expected. Until now, the recovery of LIBs has mostly been focused on the cathode because of the valuable and scarce elements, such as Co and Ni. However, it should not be ignored that graphite anode is an important strategic resource in LIBs, which accounts for around 28 wt % of LIBs and experiences an exponentially increasing depleting due to its irreplaceable outstanding chemical and physical features in LIBs.^[5,6]

The main recycling methods of graphite, as reported in the literature, are hydrometallurgy and pyrometallurgy. Graphite from spent LIBs is typically covered with a thick SEI layer and lithium dendrites, and experiences structural collapse after long-term cycling. Despite the significant energy consumption, burning out impurities and regraphitizing spent graphite at ultra-high temperatures (above 2600 °C) is a promising graphite recovery method.

To treat spent graphite, leaching agents such as HCl, H₂SO₄, citric acid, HNO₃, and H₃BO₃ are used to remove impurities, followed by low-temperature calcination to rebuild the graphite structure.^[8–15] Using the sulfate roasting method, some impurities in spent graphite were removed by transformed into their corresponding sulfate.^[16] Gao *et al.* reported that almost all impurities in spent graphite are reduced to varying extents after sulfuric acid leaching, along with an enlargement of crystallite interlayer spacing and exfoliation of graphite flakes.^[17] Crystallinity is then recovered through subsequent heat treatment at 900 °C. This regeneration process dramatically improves the structure and enhances the physical properties of spent graphite, thus improving its electrochemical properties. However, some thin microcrystallites of graphite are unavoidable after acid leaching.

[a] H. Sheng, M. Graczyk-Zajac, H. Tian, F. Qu, Y. Zhang, A. Weidenkaff, R. Riedel

Department of Materials and Earth Sciences
Technical University of Darmstadt
Otto-Berndt-Straße 3, 64287 Darmstadt, Germany
E-mail: huiying.sheng@stud.tu-darmstadt.de

[b] M. Graczyk-Zajac
EnBW Energie Baden-Württemberg AG
Durlacher Allee 93, 76131 Karlsruhe, Germany
E-mail: m.graczyk-zajac@enbw.com
graczyk@materials.tu-darmstadt.de

[c] M. Dürrschnabel
Institute for Applied Materials
Karlsruhe Institute of Technology
Hermann-von-Helmholtz-Platz 1, 76344 Eggenstein-Leopoldshafen, Germany

[d] A. Weidenkaff
Fraunhofer IWKS
Rodener Chaussee 4, 63457 Hanau, Germany

 Supporting information for this article is available on the WWW under
<https://doi.org/10.1002/batt.202400003>

 © 2024 The Authors. *Batteries & Supercaps* published by Wiley-VCH GmbH. This is an open access article under the terms of the Creative Commons Attribution Non-Commercial NoDerivs License, which permits use and distribution in any medium, provided the original work is properly cited, the use is non-commercial and no modifications or adaptations are made.

The initial coulombic efficiency of regenerated graphite in LIBs is comparably lower than the one of the pristine graphite due to structural defects induced by the regeneration even with a cost-intensive treatment.^[18] This can be avoided if alternative applications of recovered graphite in energy storage would be found. Using recovered graphite as a matrix for encapsulating sulfur cathodes in lithium-sulfur battery (LSB) represents such an option. LSBs are considered as a potential candidate to replace LIBs in the future due to several advantages: i. high theoretical energy density of up to 2600 Wh/kg. The future demand for the power battery in the future automotive industry is targeted as over 500 Wh/kg; ii. Sulfur is a cheap, non-toxic, and earth-abundant material; iii. LSBs have a different operating mechanism which diminishes the risk of a thermal runaway and thus makes this technology potentially safer.^[6,19] However, the electrically insulating nature of sulfur and lithium sulfide, its poor cycling performance caused by the "shuttle effect" leaded by the high solubility of polysulfides and the large volume changes (80%) during the redox reaction impede the use of sulfur as the cathode material.^[20] Regenerated graphite, possessing a unique combination of excellent electronic conductivity and a robust, stress-accommodating mechanical stability, represents a highly promising matrix material for sulfur cathodes. The random pore structures of regenerated graphite provide free space to decrease the load pressure caused by the volume changes during cycling. The shuttle effect caused by the dissoluble polysulfides can also be retarded by a physical encapsulation in pore structures leading to a significant improvement of coulombic efficiency and cycling stability of batteries.^[21] In addition, graphite offers a facile ion transportation related to the reaction of sulfur and polysulfides with lithium ions and compensates for poor electrical conductivity of the sulfur cathode.^[19,22–25]

In this work, spent graphite was collected from discarded 21700 cylindrical lithium-ion batteries from Samsung SDI. Sulfuric acid solutions (5 M and 18 M) were used as leaching/intercalation agents to remove the impurities and pore forming agents. Spent graphite was leached in the acid solutions and heated to 900°C at argon atmosphere to acquire a stable structure. Initial sulfur contents of 50, 67, and 85 wt% have been encapsulated into the treated graphite for electrochemical

test as the cathode of the lithium sulfur batteries. The effect of leaching with different sulfuric acid concentrations on the crystallite structure, morphology, pore size, specific surface area has been investigated. Electrochemical tests (cycling stability, rate performance, and cyclic voltammetry) have been performed to figure out the influences of the reclaimed graphite properties and sulfur contents on the electrochemical performance of the cathode material.

Results and Discussion

The carbon content quantified by elemental analysis as well as the sulfur content measured by ICP-OES are shown in Table 1. The carbon content of the RGC is higher due to the removal of impurities from spent graphite after repeated charging and discharging processes. It is notable that the sulfur loading capacity of RGC is higher than that of RG, indicating that the graphite leached in higher acid concentration results in high amount of spaces to accommodate sulfur, which is further supported by the subsequent BET results.

The XRD analysis reveals the presence of a $P6_3/mmc$ hexagonal structure in the samples SG, RG and RGC (96-101-1061). The most intensive reflection is the (002) plane located at $2\theta = 12.1$ for all the samples as depicted in Figure 1(a). A slight shift of the (002) reflex from $2\theta = 12.10$ to $2\theta = 12.12$ after acid treatment is found (see Figure 1(b)), which is caused by the reduction of crystallite size (L_c) and number of crystallite layers (n) as calculated in Table 2.^[18] The results indicate that the crystallite structure of spent graphite is still stable. The reduction of L_c and n of RG and RGC suggests some exfoliation of graphite after acid leaching and heat treatment, which can be proofed by subsequent tests. The interplanar spacing of all the samples are 0.337 nm, which is in agreement with the TEM analysis revealing 0.327 ± 0.013 nm, 0.329 ± 0.019 nm, and 0.328 ± 0.011 nm of SG, RG, and RGC, respectively as shown in Figure S1.

Raman spectroscopy measurements were performed in the range from $0 \sim 4000$ cm⁻¹. Three characteristic peaks, namely the D band (1353 cm⁻¹, A1g symmetry), G band (1577 cm⁻¹, E2g vibration symmetry), and 2D band (2722 cm⁻¹, second-order peak of D band) are found in the recorded spectra as shown in

Table 1. Sample notation, carbon content, and sulfur content of the prepared samples.

Sample notation	Carbon content (wt%)	Sulfur content (wt%)	Remark
SG	86.1	–	spent graphite
RG	86.3	–	spent graphite leached in 5 M H ₂ SO ₄
RGC	89.8	–	spent graphite leached in 18 M H ₂ SO ₄
RG-50S	44.4	50.3	spent graphite leached in 5 M H ₂ SO ₄ with 50 wt% initial sulfur
RGC-50S	43.2	52.0	spent graphite leached in 18 M H ₂ SO ₄ with 50 wt% initial sulfur
RG-66S	28.7	66.9	spent graphite leached in 5 M H ₂ SO ₄ with 67 wt% initial sulfur
RGC-66S	27.7	68.1	spent graphite leached in 18 M H ₂ SO ₄ with 67 wt% initial sulfur
RG-85S	16.5	81.9	spent graphite leached in 5 M H ₂ SO ₄ with 85 wt% initial sulfur
RGC-85S	12.9	83.9	spent graphite leached in 18 M H ₂ SO ₄ with 85 wt% initial sulfur

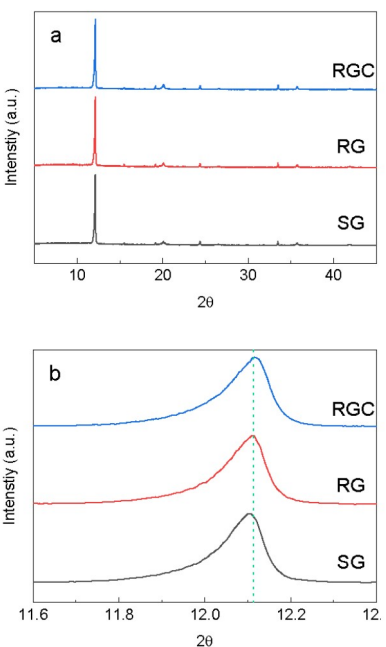


Figure 1. XRD characterization of (a) SG, RG, and RGC. (b) comparison of the (002) peak of all samples.

Table 2. Characteristics of the (002) reflex of graphite related to samples SG, RG, and RGC.					
Sample	2θ	FWHM	d (nm)	Lc (nm)	n
SG	12.104	0.132	0.337	0.540	1.601
RG	12.113	0.136	0.337	0.527	1.563
RGC	12.117	0.141	0.337	0.507	1.504

2 d sin θ = λ; θ is the Bragg angle; d represents the interplanar spacing; λ is the wavelength of Mo target (0.0711 nm). Lc = K λ / β cos θ; Lc is the vertical crystallite size of interlayer plane; K refers to the shape factor; β is the full width at half maximum (FWHM, in radian). n = Lc/d; n is the number of crystallite layers.

Figure 2. After high-concentration acid leaching, the intensity of D band remarkably increased which is caused by arising from aromatic six-fold rings. The I_D/I_G ratio of SG, RG and RGC increased with increasing disorder of the graphite due to surface defects originating from the strong acid leaching procedure as shown in Table 3. The crystallite size (L_a) and inter-

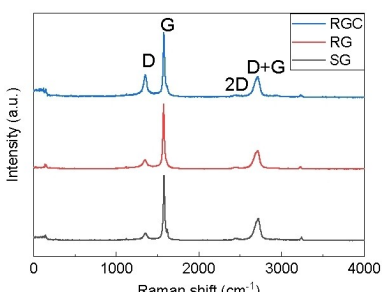


Figure 2. Raman spectra of SG, RG, RGC.

Table 3. I_D/I_G ratio, in-plane crystallite size (L_a) and inter-defect distance (L_D) of SG, RG and RGC.

Parameter	SG	RG	RGC
I_D/I_G ratio	0.24	0.51	0.65
L_a (nm)	70.07	32.97	25.87
L_D (nm)	22.92	15.73	13.93

defect distance (L_D), calculated from Equation (1) and (2), decreased as a result of small proportion of cluster formation and crystallite structure distortion after the stronger acid leaching, which demonstrated the exfoliation of graphite during acid leaching, respectively.^[26-28]

$$L_a \text{ (nm)} = (2.4 \times 10^{-10}) \lambda_1^4 (I_D/I_G)^{-1} \quad (1)$$

$$L_D^2 \text{ (nm}^2\text{)} = (1.8 \times 10^{-9}) \lambda_1^4 (I_D/I_G)^{-1} \quad (2)$$

L_a denotes in-plane crystallite size, nm; L_D denotes the average inter-defect distance, nm; I_D/I_G denotes the intensity ratio of the D band and G band; λ_1 is the laser wavelength, 514.5 nm.

SEM images illustrating the morphology of SG, RG, and RGC are shown in Figure 3. After the acid treatment, flakes and fragments (marked with red circles) are found within the samples of reclaimed graphite RG and RGC as compared to that of the spent graphite SG. These graphs show the exfoliation of graphite during the acid treatment, which aligns with the findings from the XRD and Raman data. The surface of the graphite particles appears smoother indicating the removal of the impurities after treatment with a high concentration of acid. From the EDS data (Table S1), fluorine on the surface of graphite is eliminated, while the amount oxygen is reduced due to the graphite oxidation in air. Subsequently, after sulfur infiltration, the surfaces of the graphite exhibit uniform coverage with sulfur, as illustrated in Figure S1.

The nitrogen adsorption and desorption tests of SG, RG, RGC exhibit typical type-IV isotherms indicating the presence of mesopores in all samples, as shown in Figure 4.^[29] The specific surface area, total pore volume, and average pore size of the samples slightly increase from 12.7 m²/g to 14.7 m²/g, 0.025 cm³/g to 0.03 cm³/g, and 7.8 nm to 8.0 nm, listed in Table 4, originating from the 5 M and 18 M sulfric acid leaching, respectively. These results are in good agreement with the findings of the Raman spectroscopy and SEM study. The BJH method is applied to characterize the pore size distribution of

Table 4. Specific surface area, total pore volume, and average pore size of SG, RG, and RGC.

Parameter	SG	RG	RGC
Specific surface area (m ² /g)	12.7	14.5	14.7
Total pore volume (cm ³ /g)	2.5E-2	2.8E-2	3.0E-2
Average pore size (nm)	7.8	7.7	8.0

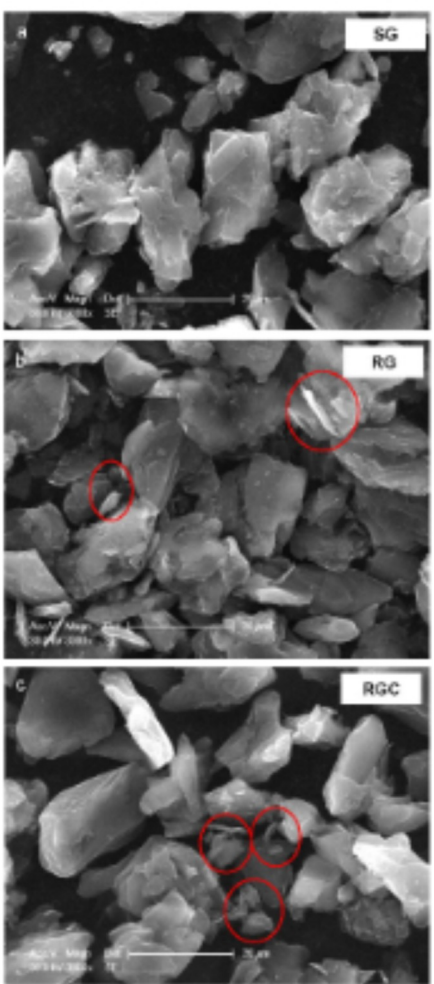


Figure 3. SEM images of (a) spent graphite; (b) reclaimed graphite leached by 5 M H_2SO_4 ; (c) reclaimed graphite leached by 18 M H_2SO_4 .

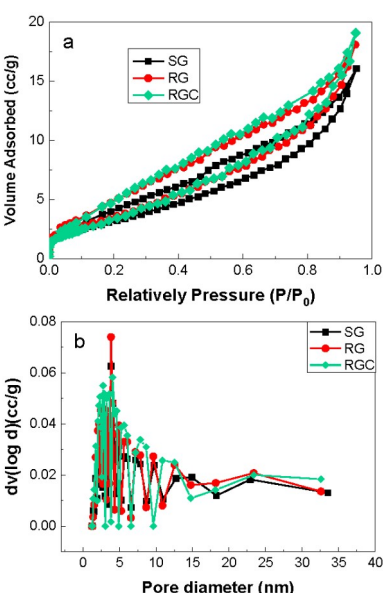
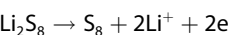
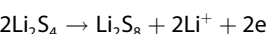
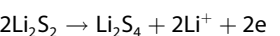


Figure 4. Nitrogen adsorption-desorption isotherms (a) and pore size distribution (b) of SG, RG, RGC.

samples. A combination of meso- and micropores is detected, with pore sizes measuring below 35 nm.

After sulfur incorporation, the amount of sulfur on the surface has been quantified by means of EDS analysis. The content of the infiltrated sulfur has been calculated from the difference between the total sulfur and surface sulfur (see in Table 5). Graphite leached with a higher acid concentration reveals the highest pore volume and thus can embed more amount of sulfur. Accordingly, the sample RGC-85S provides the highest encapsulated sulfur content of 55.1 wt %.

Galvanostatic charging/discharging measurements were performed to evaluate the capacity and cycling stability of samples. The tests were carried out at 0.1 C of a theoretical current density of 1670 mAh/g for 100 cycles. Figure 5(a) displays the first charge/discharge transients recorded for all the investigated materials, whereas Figure 5 (b,c) depict the long cycling stability of the RG and RGC samples. Two voltage plateaus are found in the initial lithiation curve at 2.3 and 2.1 V, representing the reduction of cyclo- S_8 to Li_2S_n ($4 \leq n \leq 8$) which is subsequently reduced to Li_2S_2 and Li_2S (Figure 5(a)). The delithiation reactions are represented in the charging curve with two potential plateaus at around 2.3 and 2.4 V, which are attributed to the following reactions:^[30]



There is a fast fading of the specific capacity of all the samples recorded in the first 10 cycles, originating from the formation of solid electrolyte interphase (SEI) and polysulfides dissolution. However, after the following cycles the capacity remains stable as shown in Figure 5(b,c). The RGC/S sample exhibits improved cycling stability and capacity compared to that of RG/S after 100 cycles, when the same amount of sulfur is added initially. This improvement is attributed to the high surface capacity, abundant pore structure and high defect concentration of the reclaimed RGC, as already indicated by nitrogen adsorption and Raman spectroscopy results. These characteristics provide more space for sulfur loading and create

Table 5. Summary of surface, total and infiltrated sulfur contents.

Sample	Surface S (wt%)	Total S (wt%)	Infiltrated S (wt%)
RG-50S	23.1	50.3	27.2
RG-66S	30.4	66.9	36.5
RG-85S	41.7	81.9	40.2
RGC-50S	18.0	52.0	34.0
RGC-66S	25.7	68.1	42.4
RGC-85S	28.8	83.9	55.1
Remark	Detected by EDS	Detected by ICP-OES	Calculated

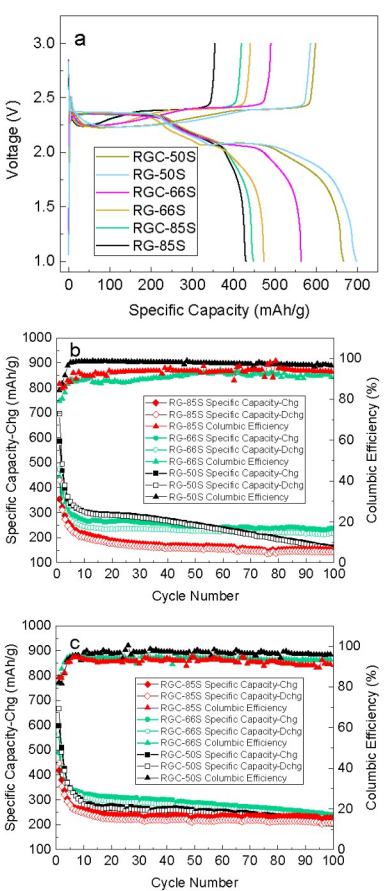


Figure 5. (a) Initial discharging and charging curve of RG-50S, RGC-50S, RG-66S, RGC-66S, RG-85S, and RGC-85S at 0.1 C. (b) Galvanostatic charge/discharge curves of RG-50S, RG-66S, and RG-85S under 0.1 C for 100 cycles. (c) Galvanostatic charge/discharge curves of RGC-50S, RGC-66S, and RGC-85S under 0.1 C for 100 cycles.

additional barriers that hinder the diffusion of polysulfides into the electrolyte. Highest sulfur loading leads to the lowest recovered capacity for RG and RGC. This is due to the excess of sulfur resulting in isolated sulfur particles, leading to the lack of electrical contact with the graphite. Therefore, these isolated sulfur particles remain inactive during the electrochemical reaction. This feature is more visible for a less porosity and lower total pore volume of RG sample. In contrast for the low sulfur loading, the initial capacity is high, however it tends to fade. Again, this feature is more pronounced for the sample RG

(see electrochemical results summarized in Table 6). Regenerated graphite with the sulfur content of 68.1 wt% shows the highest specific discharging capacity (224 mAh/g) after 100 cycles. RGC-85S with up to 83.9 wt% of sulfur content still shows a good discharging capacity (207 mAh/g) and high capacity retention (46 %) after 100 cycles which is much higher than that of RG-85S. This result suggests that graphite leached in high acid concentration is beneficial to achieve high sulfur loadings.

The resistance of the interphases and the bulk cathode material in the investigated Li–S half cells have been determined by means of Electrochemical Impedance Spectroscopy (EIS). Figure 6 shows the corresponding Nyquist plots recorded in the frequency range from 100 kHz to 0.01 Hz. The obtained results have been listed in Table 7. R_e is attributed to the electrolyte and electrical connection resistances in the high frequency region. R_{SEI+ct} corresponds to the electrolyte/electrode interphase resistance and charge transfer resistance in the middle frequency region.^[31] In general, increasing sulfur load leads to a higher resistance of the material. RGC samples show the lower charge transfer resistances than RG samples because RGC reveals a higher specific surface area providing more place for sulfur infiltration and thus faster charge transfer. The loop in middle frequency region shifts to lower value, as shown in Figure 6, which was attributed to the increase of passivation electrode/electrolyte layers, together with the active lithium polysulfides reactions. Similar trends of the semicircles and R_{SEI+ct} of samples with 67 wt% and 85 wt% of initial sulfur content are found.

Figure 7(a,b) show the rate performance of RG and RGC graphite infiltrated with 67 wt% and 85 wt% sulfur at the current range of 0.1 C to 1 C. The capacity gradually decreased with increasing current density, nevertheless a high capacity is recovered after returning to 0.1 C rate. RG and RGC with 67 wt% sulfur are more stable than samples containing 85 wt% sulfur. The average reversible specific capacity at 0.1 C, 0.2 C, 0.5 C, 1 C, and returned to 0.1 C of RGC-66S are 308, 179, 95, 36, 237 mAh/g, while those of RG-66S are 284, 173, 114, 67, 226 mAh/g, respectively, which both of them recovered their capacity after high current density. The sample RGC-66S performed slightly better than RG-66S at low current densities, except the current density rose to 0.5 C, especially 1 C. The capacity of RGC-85S is higher than that of RG-85S at each current density. This result is rationalized by the fact that a larger amount of sulfur could be infiltrated into the structure of

Table 6. Electrochemical parameters of the RG-50S, RG-66S, RG-85S, RGC-50S, RGC-66S, and RGC-85S.

Parameter	RG-85S		RG-66S		RG-50S		RGC-85S		RGC-66S		RGC-50S	
Cycling number	1	100	1	100	1	100	1	100	1	100	1	100
Specific charge capacity (mAh/g)	354	152	441	238	586	160	419	228	490	240	598	209
Specific discharge capacity (mAh/g)	430	142	474	216	697	156	448	207	564	224	666	201
CE (%)	88	93	79	91	84	96	85	91	82	93	82	96
Capacity retention (%)	33		46		22		46		40		36	

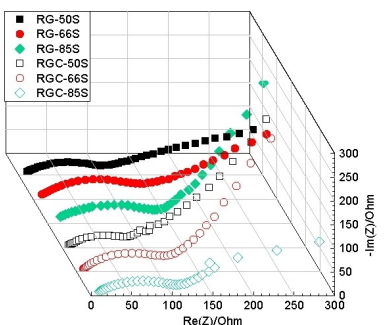


Figure 6. Nyquist plots of RG-50S, RG-66S, RG-85S, RGC-50S, RGC-66S and RGC-85S.

Table 7. Resistance results of EIS spectra at OCV state

	Open circuit voltage (OCV) state	
	R _e (Ω)	R _{SEI+ct} (Ω)
RG-50S	9.67	100.71
RG-66S	10.49	130.87
RG-85S	15.59	131.87
RGC-50S	7.73	79.69
RGC-66S	8.14	106.97
RGC-85S	9.95	105.26
	Resistance at high frequency	Resistance at median frequency

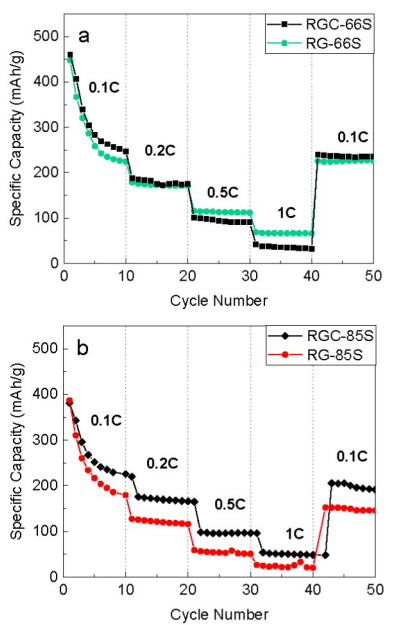


Figure 7. Rate capability of (a) RG-66S and RGC-66S, and (b) RG-85S and RGC-85S.

graphite enhancing the electronic and ionic conductivity and minimizing the shuttle effect of polysulfide.

Figure 8 shows the cyclic voltammograms recorded to get an insight about the occurring redox reactions. Figure 8(a)

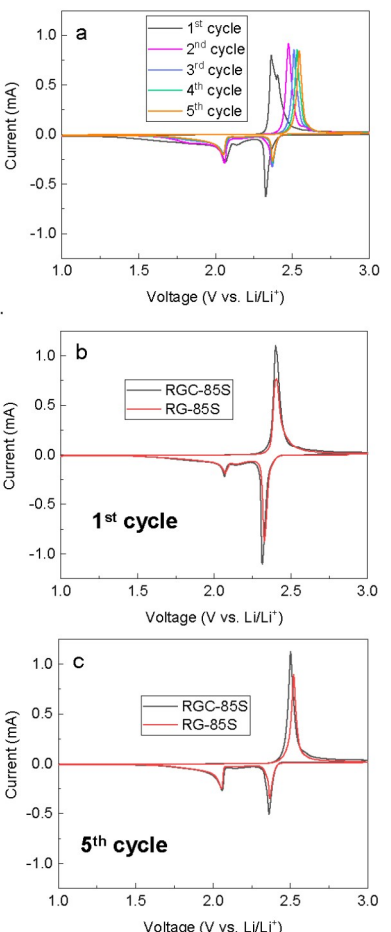


Figure 8. Cyclic voltammetry of (a) RGC-66S and the comparison of RG-85S and RGC-85S at (b) the first cycle and (c) the fifth cycle at a scan rate of 0.02 mV/s.

shows the first 5 cycles recorded for RGC-66S. In the first cycle, the cathodic peak at 2.37 V is related to the reduction of sulfur to soluble lithium polysulfides (Li_2S_n ($4 \leq n \leq 8$)), followed by a second cathodic peak at 2.05 V due to the further reduction of soluble Li_2S_n ($4 \leq n \leq 8$) to solid Li_2S_2 and Li_2S . Two anodic peaks are found at 2.36 and 2.40 V corresponding to the reverse reactions, respectively.^[32] In the second cycle, two anodic peaks overlapped into one peak. The first cathodic peak and anodic peak shift negative, along with the decreasing intensity of the cathodic peak, indicating the capacity decay and polarization of the cell.^[33–35] However, from the third cycle, no significant change of the intensity and position of the peaks is found, except a slight left move of the anodic peak, which implies a small decay of the cell during charging. Figure 8(b,c) present the comparison of the first and fifth cycles recorded for RG-85S and RGC-85S. The intensity of each peaks of RG-85S is lower than that of RGC-85S, which again explains the advanced electrochemical performance of RGC-85S. After 5 cycles, the intensity of all peaks drops down, especially the first cathodic peak. This phenomenon is also found in RGC-66S. The anodic

peak of RGC-85S is shifted to less negative potential, underlining the better electrochemical performance during cycling.

Conclusions

This work provides a facile and up-scalable way for graphite reclamation from spent LIBs and its further application as a host matrix for sulfur in lithium sulfur batteries.

Sulfuric acid leaching effectively removes impurities but also leads to the formation of a well-developed porosity capable to encapsulate significant amount of sulfur. Simultaneously, an exfoliation of graphite occurs, reducing the crystallite size and providing more defect sites. Increasing the acid concentration during the leaching process results in a higher surface area, total pore volume, and average pore size, facilitating an advanced sulfur infiltration. Among all the samples, RGC-66S displays the highest capacity retention of 224 mAh/g after 100 cycles.

This study represents a practical approach to efficiently use reclaimed graphite in LSB application other than re-utilization in LIBs.

Experimental Section

Pretreatment of Spent Graphite

The discarded lithium-ion batteries were fully discharged in a 5 % NaCl solution for 24 h and dried at room temperature before dismantling. The cells were disassembled in a glove box. Spent graphite was directly scratched from the anode current collector. The collected material was heated to 650 °C for 5 h in a muffle oven to remove the residual binder, electrolyte, and other by-products and subsequently cooled down with a cooling rate of 100 °C/h. The product was denoted spent graphite, SG.

Reclamation of Spent Graphite

The spent graphite was ground in a ball mill (MM 400, Retsch GmbH, Germany) for 5 min at a frequency of 30 Hz/s and sieved with a mesh size of 40 µm. Then, SG was immersed into the 5 M and 18 M sulfuric acid (H_2SO_4 , AR grade 96 %) solution at room temperature for 24 h with a solid-liquid ratio of 1:20. After leaching, the residues were filtered and washed with deionized water until the filtrate became a neutral pH. The leached graphite was subsequently dried overnight at 80 °C. The reclamation of graphite was carried out in a tubular resistance furnace at 900 °C for 3 h in argon atmosphere with the heating and cooling rate of 100 °C/h. Graphite leached in 5 M and 18 M sulfuric acid were denoted as reclaimed graphite RG and RGC, respectively.

Fabrication of Graphite-S Composite

Reclaimed graphite was mixed with sulfur powder (Alfa Aesar, Germany) by the mass ratio 15:85 (85 wt % of sulfur), 33:67 (67 wt % of sulfur), 50:50 (50 wt % of sulfur) via ball milling. The mixtures were then heated to 160 °C for 24 h in teflon inlets which were sealed in autoclaves. The graphite-S composites were then ground using a mortar. The sample denotations and compositions

are listed in Table 1. For example: RG-50S means reclaimed graphite leached in 5 M sulfuric acid loaded with 50 wt % sulfur.

Characterization of the Materials

The carbon content of the different samples was determined using a LECO C-200 (LECO Instrumente GmbH, Mönchengladbach, Germany). The content of sulfur was measured by inductively coupled plasma optical emission spectrometry (ICP-OES). The crystalline phases of the samples were identified via X-ray powder diffractometry (XRD, STOE STADIP, Darmstadt, Germany) at the 20 range of 5~45°, with monochromatic $Mo_{K\alpha}$ radiation ($\lambda = 0.0711$ nm). Raman spectra were acquired at ambient temperature with a micro-Raman spectrometer (Horiba HR800, Kyoto, Japan) with an argon ion laser (wavelength of 514.5 nm) as the source of excitation in air. N_2 adsorption/desorption isotherms at 77 K (Quantachrome Autosorb-3B, Boynton Beach, FL, USA) were analyzed by means of the Brunauer-Emmett-Teller method (BET) and the Barrett-Joyner-Halenda algorithm (BJH) was employed to determine the specific surface area and pore size distribution. Scanning electron microscopy was performed with a JEOL JSM 7600 F (SEM, JEOL Ltd., Chiyoda, Tokyo, Japan) with an accelerating voltage of 30 kV coupled with EDS for elemental analysis of the materials. Transmission Electron Microscopy (TEM) was carried out using a Thermo Fisher Talos F200X. The microscope was operated at 200 kV acceleration voltage. For TEM imaging a Thermo Scientific Ceta camera was used. Diffraction pattern and FFT images were indexed using the SingleCrystal software.^[36]

Electrochemical Measurements

The graphite-S composites were mixed with 5 wt % carbon black (TIMCAL Super P Conductive Carbon Black), 5 wt % carboxymethylcellulose (CMC, Sigma-Aldrich, UK), and 5 wt % styrene-butadiene rubber (SBR, ZEON, Japan) in water to increase the adhesion and mechanical stability of the slurry. The compound was printed on an aluminium foil coated with carbon, setting a thickness of 120 µm with a doctor blade. After drying of the printed electrode at 40 °C for overnight, the electrodes were cut into discs with a diameter of 10 mm. The electrodes were further dried in a vacuum oven (Büchi B-580 Glass Oven, Labortechnik AG, Germany) at 60 °C for 24 h to completely remove the humidity. The Swagelok-type cell was assembled in a glove box under argon atmosphere with the electrode, a separator QMA (Whatman GE Healthcare, Maidstone, UK), a 10 mm diameter metallic lithium foil (0.75 mm thickness, Alfa Aesar GmbH & Co KG, Karlsruhe, Germany), and 180 mL electrolyte comprised of 1 M lithium bis(trifluoromethanesulfonyl)imide (LiTFSI) in a mixture of 1,3-dioxolane (DOL)/dimethoxymethane (DME) (v/v = 1:1) with 0.1 M LiNO₃ as additive. All electrochemical tests were done at 25 °C. Galvanostatic cycling was performed on a Neware multichannel battery tester using the BTSDA software version 7.6.0.443 with potential limitation (GCPL) performed under a constant current value of 167 mA/g (0.1 C) in a voltage range between 1 V and 3 V for 100 cycles. EIS was measured for electrodes in the open circuit voltage (OCV) condition in the frequency range of 100 kHz to 0.01 Hz. Cyclic voltammetry (CV) was carried out on a Bio-Logic SP-150 cycler using the EC-Lab software version 10.12 at a scan rate of 0.02 mV/s for 5 cycles.

Acknowledgements

Huiying Sheng kindly acknowledges the financial support by the China Scholarship Council (CSC, No. 202308080034).

Honghong Tian kindly acknowledges the financial support by the China Scholarship Council (CSC, No.202009150013). Fangmu Qu acknowledges the financial support by the China Scholarship Council (CSC, No. 201904910776), Yaohao Zhang acknowledges the financial support by the China Scholarship Council (CSC, No. 202108610068). Open Access funding enabled and organized by Projekt DEAL.

Conflict of Interests

The authors declare no conflict of interest.

Data Availability Statement

The data that support the findings of this study are available from the corresponding author upon reasonable request.

Keywords: spent graphite • recycling • hydrometallurgy • lithium sulfur battery

- [1] M. Abdollahifar, P. Molaiyan, U. Lassi, N. L. Wu, A. Kwade, *Renewable Sustainable Energy Rev.* **2022**, 169, doi: 10.1016/j.rser.2022.112948.
- [2] V. Etacheri, R. Marom, R. Elazari, G. Salitra, D. Aurbach, *Energy Environ. Sci.* **2011**, 4, doi: 10.1039/c1ee01598b.
- [3] M. Abdollahifar, S. Doose, H. Cavers, A. Kwade, *Adv. Mater. Technol.* **2022**, 4, doi: 10.1002/admt.202200368.
- [4] P. Li, S. Luo, L. Zhang, Q. Liu, Y. Wang, Y. Lin, C. Xu, J. Guo, P. Cheali, X. Xia, *J. Energy Chem.* **2024**, 144, doi: 10.1016/j.jecchem.2023.10.012.
- [5] B. Niu, J. Xiao, Z. Xu, *J. Hazard. Mater.* **2022**, 439,129678, doi: 10.1016/j.jhazmat.2022.129678.
- [6] X. Yang, R. Li, J. Yang, H. Liu, T. Luo, X. Wang, L. Yang, *Carbon.* **2022**, 199, 215, doi: 10.1016/j.carbon.2022.06.067.
- [7] S. H. Beheshti, M. Javanbakht, H. Omidvar, M. S. Hosen, A. Hubin, J. Van Mierlo, M. Berecibar, *iScience* **2022**, 103862, doi: 10.1016/j.isci.2022.103862.
- [8] Y. Yang, S. Song, S. Lei, W. Sun, H. Hou, F. Jiang, X. Ji, W. Zhao, Y. Hu, *Waste Manage.* **2019**, 85, 529, doi: 10.1016/j.wasman.2019.01.008.
- [9] C. Xu, G. Ma, W. Yang, S. Che, Y. Li, Y. Jia, H. Liu, F. Chen, G. Zhang, H. Liu, N. Wu, G. Huang, Y. Li, *Electrochim. Acta* **2022**, 415, 140198, doi: 10.1016/j.electacta.2022.140198.
- [10] Y. Gao, C. Wang, J. Zhang, Q. Jing, B. Ma, Y. Chen, W. Zhang, *ACS Sustainable Chem. Eng.* **2020**, 8, 9447, doi: 10.1021/acssuschemeng.0c02321.
- [11] H. Li, J. Peng, P. Liu, W. Li, Z. Wu, B. Chang, X. Wang, *J. Electroanal. Chem.* **2023**, 932, 117247 doi: 10.1016/j.jelechem.2023.117247.
- [12] Q. Chen, L. Huang, J. Liu, Y. Luo, Y. Chen, *Carbon* **2022**, 189, 293, doi: 10.1016/j.carbon.2021.12.072.
- [13] J. Yang, E. Fan, J. Lin, F. Arshad, X. Zhang, H. Wang, F. Wu, R. Chen, L. Li, *ACS Appl. Energ. Mater.* **2021**, 4, 6261, doi: 10.1021/acsadm.1c01029.
- [14] Y.-J. Xu, X.-H. Song, Q. Chang, X.-L. Hou, Y. Sun, X.-Y. Feng, X.-R. Wang, M. Zhan, H.-F. Xiang, Y. Yu, *New. Carbon. Mater.* **2022**, 37, 1011, doi: 10.1016/s1872-5805(22)60648-6.
- [15] B. Markey, M. Zhang, I. Robb, P. Xu, H. Gao, D. Zhang, J. Holoubek, D. Xia, Y. Zhao, J. Guo, M. Cai, Y. S. Meng, Z. Chen, *J. Electrochem. Soc.* **2020**, 167, 160511, doi: 10.1149/1945-7111/abcc2f.
- [16] X. Zhang, D. Wang, H. Chen, L. Yang, Y. Yu, L. Xu, *Solid State Ionics* **2019**, doi: 10.1016/j.ssi.2019.05.018.
- [17] Y. Gao, J. Zhang, H. Jin, G. Liang, L. Ma, Y. Chen, C. Wang, *Carbon.* **2022**, 189, 493, doi: 10.1016/j.carbon.2021.12.053.
- [18] H. Tian, M. Graczyk-Zajac, D. M. De Carolis, C. Tian, E. I. Ricohermoso, Z. Yang, W. Li, M. Wilamowska-Zawlocka, J. P. Hofmann, A. Weidenkaff, R. Riedel, *J. Hazard. Mater.* **2023**, 445, 130607, doi: 10.1016/j.jhazmat.2022.130607.
- [19] M. Zhao, B. Q. Li, X. Q. Zhang, J. Q. Huang, Q. Zhang, *ACS Cent. Sci.* **2020**, 6, 1095, doi: 10.1021/acscentsci.0c00449.
- [20] L. Yuan, H. Yuan, X. Qiu, L. Chen, W. Zhu, *J. Power Sources.* **2009**, 189, 1141, doi: 10.1016/j.jpowsour.2008.12.149.
- [21] J. Guo, Y. Xu, C. Wang, *Nano Lett.* **2011**, 11, 4288, doi: 10.1021/nl202297p.
- [22] A. Manthiram, Y. Fu, S. H. Chung, C. Zu, Y. S. Su, *Chem. Rev.* **2014**, 114, 11751, doi: 10.1021/cr500062v.
- [23] F. Qu, Z. Yu, M. Krol, N. Chai, R. Riedel, M. Graczyk-Zajac, *Nanomaterials* **2022**, 12, 1283, doi: 10.3390/nano12081283.
- [24] F. Qu, M. Graczyk-Zajac, D. Vrankovic, N. Chai, Z. Yu, R. Riedel, *Electrochim. Acta* **2021**, 384, 138265, doi: 10.1016/j.electacta.2021.138265.
- [25] S.-C. Han, M.-S. Song, H. Lee, H.-S. Kim, H.-J. Ahn, J.-Y. Lee, *J. Electrochem. Soc.* **2003**, 150, A889, doi: 10.1149/1.1576766.
- [26] L. G. Cançado, K. Takai, T. Enoki, M. Endo, Y. A. Kim, H. Mizusaki, A. Jorio, L. N. Coelho, R. Magalhães-Paniago, M. A. Pimenta, *Appl. Phys. Lett.* **2006**, 88, 163106, doi: 10.1063/1.2196057.
- [27] L. G. Cancado, A. Jorio, E. H. Ferreira, F. Stavale, C. A. Achete, R. B. Capaz, M. V. Moutinho, A. Lombardo, T. S. Kulmala, A. C. Ferrari, *Nano Lett.* **2011**, 11, 3190, doi: 10.1021/nl201432g.
- [28] A. C. Ferrari, J. Robertson, *Phys. Rev. B* **2000**, 61, 14095.
- [29] K. S. W. Sing, *Pure Appl. Chem.* **1985**, 57, 603, doi: doi:10.1351-pac198557040603.
- [30] X. Huang, Z. Wang, R. Knibbe, B. Luo, S. A. Ahad, D. Sun, L. Wang, *Energy Technol.* **2019**, 1801001, doi: 10.1002/ente.201801001.
- [31] S. Waluś, C. Barchasz, R. Bouchet, F. Alloin, *Electrochim. Acta* **2020**, 359, 136944, doi: 10.1016/j.electacta.2020.136944.
- [32] Z. Li, Y. Jiang, L. Yuan, Z. Yi, C. Wu, Y. Liu, P. Strasser, Y. Huang, *ACS Nano.* **2014**, 8, 9295, doi: 10.1021/nn503220h.
- [33] Z. Cheng, Z. Xiao, H. Pan, S. Wang, R. Wang, *Adv. Energy Mater.* **2018**, 8, 1702337, doi: 10.1002/aenm.201702337.
- [34] X. Gao, D. Zhou, Y. Chen, W. Wu, D. Su, B. Li, G. Wang, *Commun. Chem.* **2019**, 2, doi: 10.1038/s42004-019-0166-8.
- [35] H. Peng, Y. Zhang, Y. Chen, J. Zhang, H. Jiang, X. Chen, Z. Zhang, Y. Zeng, B. Sa, Q. Wei, J. Lin, H. Guo, *Mater. Today Energy* **2020**, 18, 10519, doi: 10.1016/j.mtener.2020.100519.
- [36] SingleCrystal™: a single-crystal diffraction program for Mac and Windows. CrystalMaker Software Ltd, Oxford, England (www.crystalmaker.com).

Manuscript received: January 4, 2024

Revised manuscript received: February 19, 2024

Accepted manuscript online: March 20, 2024

Version of record online: April 29, 2024